Escola de Primavera de Transição e Turbulência
Blumenau 2020

ABCM Associação Brasileira de Engenharia e Ciências Mecânicas

12th Spring School on Transition and Turbulence
September 21st-25th, 2020, Blumenau, SC, Brazil

EPTT-2020-0109
DIRECT NUMERICAL SIMULATION OF BI-DISPERSE PARTICLE-LADEN GRAVITY CURRENTS ON LOCK-EXCHANGE CONFIGURATION WITH DIFFERENT SCHMIDT NUMBER

Guilherme Torres Marques Vidal
Gabriel Narváez Campo
Rubem Mário Figueiró Vargas
Jorge Hugo Silvestrini
Pontifícia Universidade Católica do Rio Grande do Sul, Av. Ipiranga, 681, Porto Alegre, RS
guilherme_torres@hotmail.com.br, gabriel.narvaez.campo@gmail.com, rvargas@pucrs.br, jorgehs@pucrs.br

Abstract. *We performed direct numerical simulations (DNS) of bi-disperse particle-laden gravity currents on a lock-exchange configuration with different values of Schmidt number (Sc) for each particle fraction, to investigate the impact of double mass diffusivity on flow dynamics and deposition. We used the high-order code Incompact3d to solve the incompressible Navier-Stokes equations and the scalar transport equation. We compared our results with previous physical and numerical experiments available in the bibliography, obtaining a good agreement. We simulated two cases: (i) $Sc = 1$ for both particle fractions and (ii) $Sc = 3$ and $Sc = 1$, for coarse and fine fraction, respectively. Case (ii) shows higher reduction of the front velocity of current during the deceleration phase. For case (i), the current has higher amount of suspended fine particle during all the experiment, which could explain why the front velocity has lesser decreasing during the deceleration phase. The configuration of the final deposit profile shows that case (ii) has the highest deposit peak nearer to the lock-exchange gate than the case (i). We also calculated the temporal evolution of the energy budget of our simulations, and we find that the energy is conserved during all time of our simulations and the term relate to turbulent dissipation is the principal responsible for energy loss.*

Keywords: *Bi-disperse current, particle-laden gravity current, direct numerical simulation, high-order numerical simulation, deposition of particles.*

1. INTRODUCTION

Gravity currents are created when there is a gradient of pressure between two fluids due to difference of density. When the main gradient is in horizontal direction, one fluid propagates horizontally through the other. The variation of density could be caused by a difference of temperature, salinity or suspended particles in a fresh fluid. Gravity currents are formed in many different natural situations as well as human-made. Some examples (see Fig. 1) of natural situations are thunderstorm outflows, sea-breeze fronts, airborne snow, sandstorms, powder snow avalanches and pyroclastic flows. In the ocean, these flows are driven by salinity and temperature inhomogeneities, or like in turbidity currents whose density gradients derive from suspended mud or silt. There are essential applications in different areas like aircraft safety, entomology and pest control, and in pollutants spreading into the atmosphere, lakes, and rivers. In a industry context, these flows can be observed in the manufacturing process of sheet glass. In a engineering context, these flows can destroy submarine pipes and cables (Simpson, 1982).

The particle-laden gravity currents are an example of flow caused by the presence of suspended particles in a fresh fluid. This kind of current is considered non-conservative because particle sedimentation decreases the gradient of density between the flow and the surrounding fluid. This behaviour is very different from conservative currents, where the gradient of density is created by temperature or salinity differences, and there is no sedimentation. In a geophysical context, particle-laden currents are an essential mechanism for sediment transport from shallow to deep water. In the offshore environment, non-conservative currents of sand could form deposits with great potential of being hydrocarbon reservoirs as the oil reservoirs in the pre-salt layer, for instance (Meiburg and Kneller, 2010; Lucchese, 2018).

The behaviour of gravity currents can be understood through physical experiments (Simpson, 1972; Huppert and Simpson, 1980; Manica, 2009) or numerical simulation (Kubo, 2004; Cantero *et al.*, 2007). The studies of Winters *et al.* (1995), Necker *et al.* (2005) and Espath *et al.* (2014) develop a methodology to calculate the energy budget of the flow. They perform numerical simulation of mono-disperse gravity currents and, demonstrate the relationship between each term involved in the energy budget and other global quantities like front position, suspended mass and final deposit

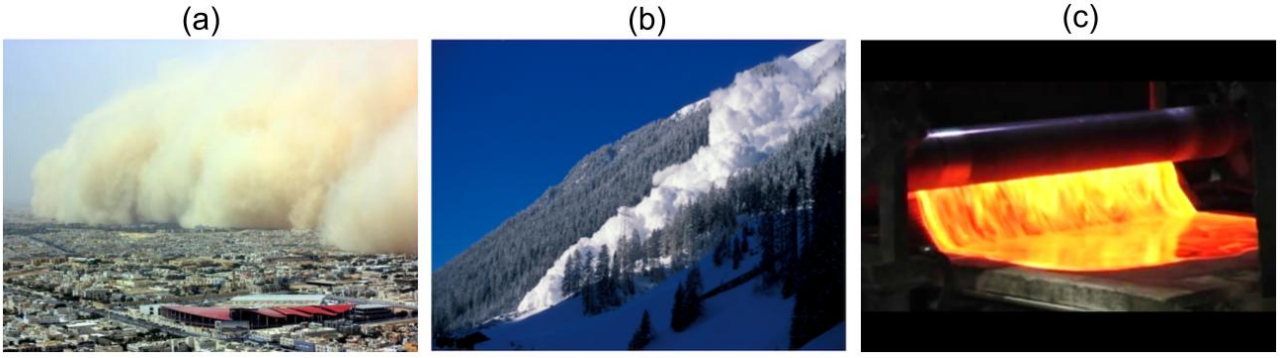

Figure 1. Some examples of gravity currents: (a) sandstorms (source: G1), (b) mountain snow avalanche (source: ESA) and (c) manufacturing of sheet glass (source: KOG).

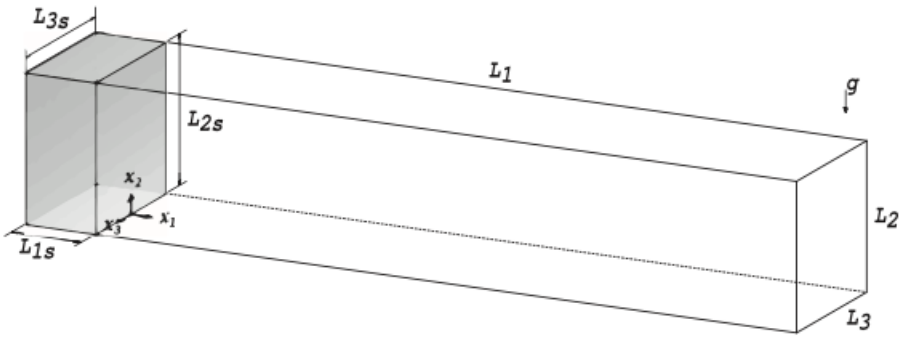

Figure 2. Schematic view for the initial configuration of lock-exchange flow. The mixture of particles and fluid is initially in the lock, filled region. Source: Francisco *et al.* (2017).

profile. The interaction of a particle-laden flows with three-dimensional topography was studied by Nasr-Azadani *et al.* (2016) through numerical simulations. Lucchese (2018) analyzed the influence of alteration of bottom topography for poly-disperse flows in a numerical context. In a experimental context, Gladstone *et al.* (1998) made experiments of poly-disperse flows to understand the impact of initial mixture of different particle fraction in current dynamics. They found that different initial concentrations had a strong impact in the features of the flow.

In a numerical context, Francisco *et al.* (2017) studied bi-dispersed particle-laden gravity in the lock-exchange configuration. Their work analyzed the impact of the initial concentration of different particle diameters in the main features of the flow. Their results show that high concentration of fine particles makes the current reach larger distances when comparing to flows with greater concentration of coarse particles. Their study used a unique unitary Schmidt number in all their simulations. In this paper, we want to extend their study by adding the effect of double mass diffusivity.

Our goal in this research is to understand the effect of different values of Schmidt number, for each particle fraction, on non-conservative and bi-disperse gravity currents, through the measurement of some flow and deposit variables as front position and velocity, suspended material, mass sedimentation rate and deposit profile. We also compute the temporal evolution of the energy budget of the current. We use the in-house code *Incompact3d* to simulate (by *DNS*) bi-disperse and double diffusive particle-laden gravity currents in lock-exchange configuration (see Fig. 2), for a Reynolds number of 4000. We perform numerical experiments at the same initial concentration of coarse and fine fraction particle for unique and different values of Schmidt number. Our approach only considers the particle deposition, ignoring erosion and re-suspension. We compare our data with previous physical and numerical experiments presented in the literature.

2. METHODOLOGY

In this section we describe the governing equations, the flow configuration as well as the treatment for the data post-processing.

2.1 Flow configuration and governing equations

The lock-exchange flow configuration in a confined channel is used in this numerical study. This arrangement consists of a homogeneous mixing of sediment and fresh fluid which are trapped in an initial fraction of the dimension domain, separated from the clear fluid by a gate. When simulation begins, the gate is removed and the particle-fluid mixing flow

due to the gravity action. Two mechanisms are responsible for motion: the first one is the transformation of potential energy into kinetic energy, the second one is the diffusive motion that is generated by the potential difference between heavy and clear fluid.

To evaluate the flow motion, we solve numerically the incompressible Navier-Stokes equations and the scalar (sediment) transport equation under the Boussinesq approximation. The dimensionless equations can be written as

$$\frac{\partial u_i}{\partial x_i} = 0, \tag{1}$$

$$\frac{\partial u_i}{\partial t} + u_j \frac{\partial u_i}{\partial x_j} = -\frac{\partial p}{\partial x_i} + \frac{1}{Re}\frac{\partial^2 u_i}{\partial x_j \partial x_j} + c_t e_i^g, \tag{2}$$

$$\frac{\partial c_l}{\partial t} + \left(u_j + u_l^s e_j^g\right)\frac{\partial c_l}{\partial x_j} = \frac{1}{Sc_l Re}\frac{\partial^2 c_l}{\partial x_j \partial x_j} \qquad l = 1, ..., N, \tag{3}$$

where u_i, p and c_l are respectively velocity, pressure and total particle concentration fields. c_t is the total particle concentration. i and j are the indexes for each spatial coordinate. $e_i^g = (0,\ -1,\ 0)$ is the unitary vector acting in the direction of the gravitational acceleration. u_l^s is the settling velocity of the particle fraction l related to its diameter. N is the total number of particles fractions in the current, being each fraction characterized by a different diameter. As in this study, all our simulations were bi-disperse, then $N = 2$. The Reynolds and Schmidt numbers are respectively defined by

$$Re = \frac{\tilde{u}_b \tilde{h}}{\tilde{\nu}}, \tag{4}$$

$$Sc_l = \frac{\tilde{\nu}}{\tilde{k}_l}, \tag{5}$$

where $\tilde{u}_b$, $\tilde{h}$ and $\tilde{\nu}$ are the buoyancy velocity, the characteristic length scale (corresponding to the lock-exchange height) and the kinematic viscosity coefficient, respectively. Sc_l and $\tilde{k}_l$ respectively are the Schmidt number and the mass diffusivity coefficient for the particle fraction l.

The total particle concentration, is obtained by the sum of each particle fraction

$$c_t = \sum_{l=1}^{N} c_l \qquad l = 1, ..., N. \tag{6}$$

As the c_t is already normalized by the total initial concentration of the mixture, in the initial configuration (Fig. 2), the sum of all particle fractions is 1 in the lock region and 0 at the rest of the domain.

A Cartesian mesh with $n_1 \times n_2 \times n_3$ grid points is used in a domain of size $L_1 \times L_2 \times L_3$. For the velocity field, we apply no-slip boundary condition at the bottom of domain, periodic conditions at $x_3 = 0$ and $x_3 = L_3$, and free-slip conditions for the other boundaries. For the scalar field, we used null normal gradient boundary condition on $x_1 = 0$ and $x_1 = L_1$, periodic condition at $x_3 = 0$ and $x_3 = L_3$, and no-flux at $x_2 = L_2$. In order to take into account the particles deposition in the vertical direction at the bottom of the domain, the following outflow boundary condition is used,

$$\frac{\partial c_l}{\partial t} + u_l^s e_2^g \frac{\partial c_l}{\partial x_2} = 0. \tag{7}$$

This condition allows to mimic the process of sediment leaving the computational domain when it touches the bottom wall. A perturbation on the velocity field at the interface between the two fluid is applied to simulate the effect of removing the gate. We use a white noise with 10% of the initial potential energy of the current with a initial perturbation.

In natural flows, as salt mixtures, the Schmidt number could be very high and computationally expensive to simulate. Moreover, for particle-laden flows, the mass diffussivity coefficient representative of the mixture, is not well defined. To overcome this problem, we use an estimation based on the diffusivity coefficient for each particle fraction, considering the Einstein-Stokes equation,

$$k_l = \frac{k_B T}{6\pi\mu r_l}, \tag{8}$$

where k_B is the Boltzmann's constant, T is the absolute temperature, μ is the dynamic viscosity coefficient and r_l is the radius of each particle fraction l. Then, applying the ratio between the Schmidt number of the two particles and considering the Eq. (8), we obtain a relation between the ratio of Schmidt number and the radius of each particle fraction,

$$\frac{Sc_1}{Sc_2} = \frac{k_2}{k_1} = \frac{r_1}{r_2}. \tag{9}$$

We propose in this paper to apply this ratio in a simulation, which means employing two Schmidt numbers, one for each particle fraction.

2.2 Software

We used the in-house code *Incompact3d* (www.incompact3d.com) to solve the incompressible Navier-Stokes equation and scalar transport equation presented above. This code employs a compact sixth-order finite difference scheme for spatial differentiation and a third-order Adam-Bashforth scheme for time integration. To apply the incompressibility condition, a fractional step method requires to solve a Poisson equation. This equation is fully solved in spectral space via the use of relevant 3D Fast Fourier Transforms. For more information about the numerical code and the parallel strategy used for *Incompact3d*, we recommend Laizet and Lamballais (2009) and Laizet and Li (2011).

2.3 Post-processing

In order to quantify the impact of double mass diffusivity in the numerical experiments, we calculate the current front position and velocity, the suspended mass, the sedimentation rate, the deposit height and the temporal evolution of energy budget of the flow. These quantities are computed at post-processing stage. Part of the post-processing step is embedded in the code *Incompact3d*, and the other part was carried out by using the programming language *Python* with some functions of libraries *Numpy* and *SciPy* for numerical integration. In this section, we are going to explain each method that we used in this step.

2.3.1 Evolution of current front position and velocity

To measure the current front position, x_f, we follow a procedure using a vertical and span-averaged total concentration defined as

$$\overline{c}_t\left(x_1,t\right)=\frac{1}{L_2L_3}\int_0^{L_2}\int_0^{L_3}c_t\,dx_2dx_3 \tag{10}$$

with this definition, the flow front position in our configuration is computed as the most forward point at x_1 where the averaged total concentration overcomes a threshold value which, in our calculations, is 0.1%.

Usually, the flow front velocity, u_f, is measured by calculating the derivative of the front position. Unfortunately, the frequency that we save the data of our simulations introduces some noise, compromising the interpretation and reducing the accuracy when we apply this method. Because of that, we choose to use the recent method proposed by Farenzena (2020). This method determines the velocity of the front as the maximum point of an integral quantity. The reference velocity $\overline{u}$ in each point of the domain is defined as

$$\overline{u}\left(x_1,t\right)=\frac{\displaystyle\int_0^{L_3}\int_0^{L_2}\left(u_1c_t-\sum_{l=1}^{N}\frac{1}{ReSc_l}\frac{\partial c_l}{\partial x_1}\right)dx_2dx_3}{\displaystyle\int_0^{L_3}\int_0^{L_2}c_tdx_2dx_3}\qquad l=1,...,N. \tag{11}$$

The front velocity is estimated as the $\overline{u}$ maximum value inside the head flow

$$u_f\left(t\right)=max\left[\overline{u}\left(-L_{head}<x_1-x_f<0,t\right)\right], \tag{12}$$

where L_{head} is the size of current head.

2.3.2 Suspended mass and sedimentation rate

We also analyse the temporal evolution of the suspended material and the sedimentation rate. The suspended mass is computed as the volume integral of the total concentration in all the domain, Ω, for each particle fraction,

$$m_{p_l}\left(t\right)=\int_\Omega c_l\,d\Omega\qquad l=1,...,N, \tag{13}$$

where m_{p_l} is the suspended mass for particle fraction l. The following equation gives the temporal evolution of sedimentation rate, $\dot{m}_{s_l}$, for the particle fraction l

$$\dot{m}_{s_l}\left(t\right)=\frac{1}{L_1L_3}\int_0^{L_1}\int_0^{L_3}c_{w_l}\left(x_1,x_3,t\right)u_l^s dx_3dx_1\qquad l=1,...,N, \tag{14}$$

where c_{w_l} is the concentration at the bottom of the domain ($x_2=0$).

2.3.3 Deposit mean profile and composition

In the numerical formulation, we impose at the bottom of the domain, the boundary condition defined in Eq. (7) to ensure that the sediments leave the computational domain throughout the simulation. Therefore, it is possible to calculate the mass deposited by the sedimentation process by integrating the mass flux through the bottom over time. The mass deposited profile, of particle fraction l, after a time t, is obtained by

$$D_l\left(x_1,t\right) = \int_0^t < c_{w_l(x_1,\tau)} >_{x_3} u_l^s d\tau \qquad l = 1, ..., N, \tag{15}$$

where $< . >_{x_3}$ operator denotes spanwise averaging. The profile of total mass deposited is expressed by

$$D_t\left(x_1,t\right) = \sum_{i=1}^{N} D_l\left(x_1,t\right) \qquad l = 1, ..., N \tag{16}$$

in this equation, the contribution of each particle fraction to the deposit can be quantified by the ratio of D_l and D_t, as it follows

$$P_l = \frac{D_l}{D_t} \qquad l = 1, ..., N \tag{17}$$

where P_l is the portion of each particle fraction in the total deposit.

2.3.4 Energy budget of the flow

The potential energy inside the lock is turned into kinetic energy after the release of the gate. In the works of Winters *et al.* (1995) and Necker *et al.* (2005) were discussed methods to calculate the temporal evolution of energy budget of gravity currents. In this work we follow the methodology used by Espath *et al.* (2014) to calculate the energy budget of the flow. This energy budget can be derived from the Navier-Stokes and scalar transport equations. The total energy can be split into kinetic and potential energy, and distinguish the dissipation associated to the strain rate in the macroscopic advective motion and the dissipation that occurs in the microscopic Stokes flows around the particles.

The kinetic energy, k, is computed by the inner product of velocity field integrated in the entire domain,

$$k\left(t\right) = \int_\Omega \frac{1}{2} u_i u_i \, d\Omega. \tag{18}$$

Differentiating Eq. (18) with respect to time and applying Eq. (2) we have

$$\frac{dk}{dt} = -\int_\Omega \frac{2}{Re} s_{ij} s_{ij} \, d\Omega - \sum_{l=1}^{N} \int_\Omega u_2 c_l \, d\Omega \tag{19}$$

where s_{ij} is the strain rate tensor give by $s_{ij} = \frac{1}{2}\left(\frac{\partial u_i}{\partial x_j} + \frac{\partial u_j}{\partial x_i}\right)$.

The expression for total potential energy is given by

$$E_{p_t}\left(t\right) = \sum_{l=1}^{N} \int_\Omega c_l x_2 d\Omega. \tag{20}$$

Taking the derivative of this expression with respect to time and applying Eq. (3), we have

$$\frac{dE_{p_t}}{dt} = \sum_{l=1}^{N} \left[\int_\Omega \left(x_2 \frac{1}{Sc_l Re} \frac{\partial^2 c_l}{\partial x_2 \partial x_2} + x_2 u_l^s \frac{\partial c_l}{\partial x_2} \right) d\Omega + \int_\Omega u_2 c_l \, d\Omega \right]. \tag{21}$$

From Equations (19) and (21) we can derive an expression for the time variation of total mechanical energy

$$\frac{d\left(k + Ep_t\right)}{dt} = -\int_\Omega \frac{2}{Re} s_{ij} s_{ij} d\Omega + \sum_{l=1}^{N} \left[\int_\Omega \left(x_2 \frac{1}{Sc_l Re} \frac{\partial^2 c_l}{\partial x_2 \partial x_2} + x_2 u_l^s \frac{\partial c_l}{\partial x_2} \right) d\Omega \right] = -\epsilon - \epsilon_{st} \tag{22}$$

where ϵ is associated to the turbulent dissipation rate and ϵ_{s_t} is the dissipation rate associated with loss of energy due to suspended particles. To compute the energy dissipated after a time t, we use

$$E_d\left(t\right) = \int_0^t \epsilon\left(\tau\right) d\tau, \tag{23}$$

$$E_{s_t}(t) = \sum_{l=1}^{N} E_{s_l}(t) = \sum_{i=1}^{N} \left[\int_0^t \epsilon_{s_l}(\tau)\, d\tau \right], \tag{24}$$

where E_{s_l} is the energy dissipated by effect of suspended particles. Finally, the complete energy equation is

$$k + E_{p_t} + E_d + E_{s_t} = E_{t_0}, \tag{25}$$

where E_{t_0} is the initial total energy, which can be get by calculate each term of the equation at $t = 0$.

2.4 Global Parameters

We performed numerical simulations of particle-laden gravity currents in a lock-exchange configuration with a fixed Reynolds number of 4000. We consider for the coarse and the fine particle fraction radius of 69 μm and 25 μm, respectively, which are the same values used in the study of Gladstone *et al.* (1998). We adopted the settling velocities of $u_1^s = 0.03$ and $u_2^s = 0.004$, for coarse and fine particle fractions, respectively. We use a computational domain size of $(L_1, L_2, L_3) = (30,\ 2,\ 0.1)$ with a number of grid points of $(n_1,\ n_2,\ n_3) = (2305,\ 325,\ 7)$. For all cases, the total simulation time was $t = 100$ with a time step of $\Delta t = 6.23 \times 10^{-4}$. For this paper, we choose two of our numerical experiments to compare with previous results presented in the literature, for the same initial concentration of coarse and fine particle of $\phi_1 = 50\%$ and $\phi_2 = 50\%$, respectively. The first one $(\#1)$ the Schmidt number for both particles fraction was equal to 1. For the second $(\#2)$, the Schmidt number of coarse and fine fraction were $Sc_1 = 3$ and $Sc_2 = 1$. According to Eq. (9), we obtain a ratio of $\frac{Sc_1}{Sc_2} = 3$.

3. RESULTS

In this section we describe the results of our simulations in terms of front position and velocity, mass suspended, deposition rate, deposit profile (in mass) and energy budget.

3.1 Evolution of current front position and velocity

According to Huppert and Simpson (1980) the gravity currents can pass by three states after flow starts. The first occurs after the gate is removed and the fluid inside the lock flows towards the streamwise direction. At this phase, the ambient fluid creates a counter-flow to the current motion that retards its movement. During this so-called slumping phase, the current front moves with constant velocity. This regime may be followed by an inertial phase where the buoyancy forces are balanced by inertial forces. At this stage, the front velocity is no more constant and starts suffering deceleration. The final regime is the viscous phase, where the buoyancy forces are balanced by viscous forces.

In Figure 3, the temporal evolution of the front position of the current is plotted, where the gate location is the initial position. We can observe a good agreement between our results and the reference for the initial time ($t < 20$). The difference for $t > 20$ related to Gladstone *et al.* (1998) is explained due to the higher Reynolds number ($Re \approx 24000$) in the experimental work. Moreover there is possibility of re-suspension at this Re number. It should be pointed out that the reference for simulation $\#1$ is the work of Francisco *et al.* (2017) which uses $Sc = 1$. On the other hand, up to $t \approx 18$, the front position of simulations $\#1$ and $\#2$ is very similar, suggesting no effect of double mass diffusivity on flow dynamics in this interval. After this period the front velocity decreases, and a noticeable difference between these two simulations appears, being the front current of simulation $\#1$ ahead when compared with simulation $\#2$. This situation remains throughout the simulation.

Figure 4 shows the temporal evolution of front velocity for the two current simulations. Three phases (Cantero *et al.*, 2007) are observed: (i) an initial almost constant regime, (ii) followed by a state in which the front velocity starts suffering deceleration, due to particle settling, at a rate of $\approx t^{-\frac{1}{3}}$ and (iii) a final regime where the velocity decrease with a rate of $\approx t^{-\frac{4}{5}}$. Both simulations show similar velocity until $t \approx 18$. When viscous effects start to be appreciable ($t > 18$), the deceleration phase starts, thus we can identify the effect of double mass diffusivity on flow dynamics, since, simulation $\#2$ seems to develop lower velocity (at least for a short period of time) than simulation $\#1$ and this situation persists until $t \approx 35$. Looking back at Eq. (3), one reason this happens is the fact that increasing the Schmidt number reduces the effect of the diffusivity term in the flow and the convective term gains more importance being the only one promoting the current movement.

3.2 Suspended mass and sedimentation rate

In Figure 5 the temporal evolution of suspended mass for coarse (m_{p_1}) and fine (m_{p_2}) particle fractions is plotted. All curves are normalized by the initial material suspended (m_{p_0}). The suspended mass shows a good agreement with the reference. The suspended mass of *coarse particles* starts at the initial concentration of 50% followed by a quick drop reaching values less than 10% of m_{p_0} at $t \approx 20$ (Fig. 5a). Moreover, simulations $\#1$ and $\#2$ are very close until $t \approx 40$ from which simulation $\#2$ shows a slightly higher amount of coarse particles suspended. For the suspended material

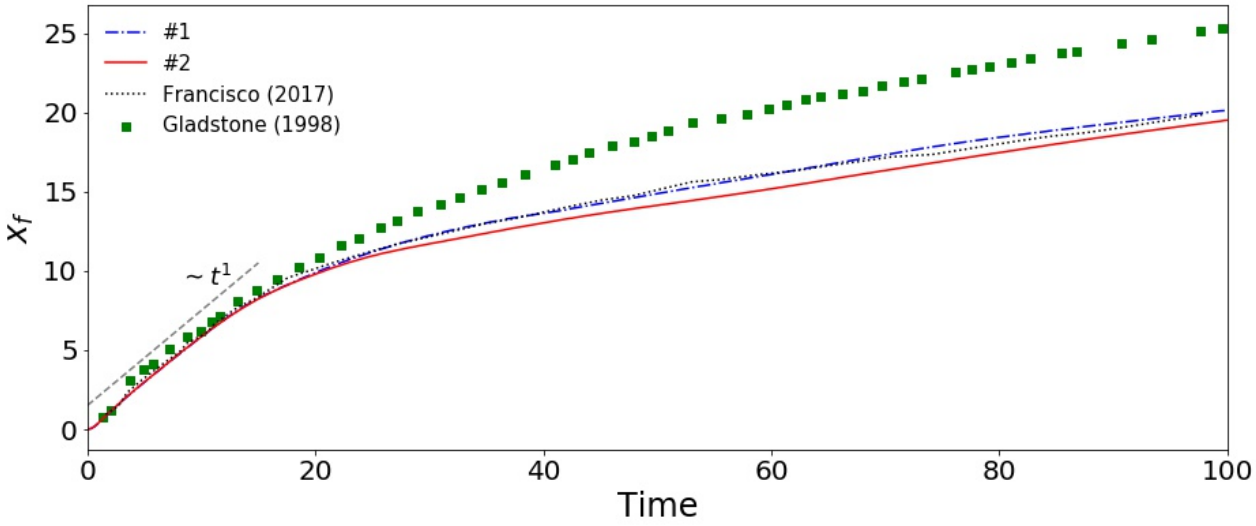

Figure 3. Time evolution of the front position of the current for simulations #1 and #2 compared with the reference. The initial position is considered at the gate location.

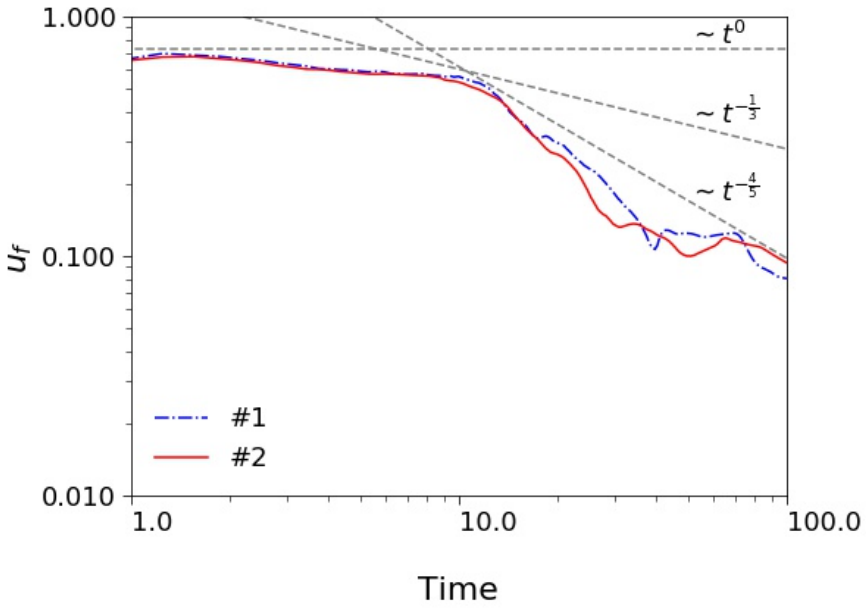

Figure 4. Time evolution of the front velocity of the current for simulations #1 and #2.

of *fine particles*, the curves decrease slower when compared to coarse particles. The simulations are very similar until $t \approx 20$, at this point the curve for simulation $\#2$ has a larger decrease when comparing against simulation $\#1$, and remains lower for the rest of simulation. This suggests a slight impact of the double mass diffusivity in the amount and particle fraction of suspended mass. This behaviour could help to explain the results on front position and velocity, since the fine particles are the most responsible for keeping the flow motion and reaching higher distances, due to the coarse particles have a greater settling velocity depositing more quickly. This is because the fine particles remains for more time suspended, maintaining the density gradient. This has been demonstrated physically (Gladstone *et al.*, 1998) as well as numerically (Francisco *et al.*, 2017). Thus, as simulation $\#1$ has more fine particles suspended during the experiment, it could explain why, after most of the coarse sediments are already deposited, the front position remains ahead if compared with the simulation $\#2$.

The sedimentation rate gives the history of sediments that leave the computational domain at the bottom. Figure 6 shows the sedimentation rate for coarse and fine particle fraction as a function of time, showing a good agreement between our results and the reference. Two distinct phases (Francisco *et al.*, 2017) can be identified: in the first phase, the curve increases proportionally to $\approx t^{0.4}$ until it reaches a maximum value around $t \approx 15$ (globally, the simulation $\#2$ has higher sedimentation rate than simulation $\#1$); in the following phase, the curve suffers a sharp decrease at a rate of $\approx t^{-3.25}$. In this last phase, both simulations are similar, but simulation $\#2$ shows lower sedimentation rate in some instants. For the

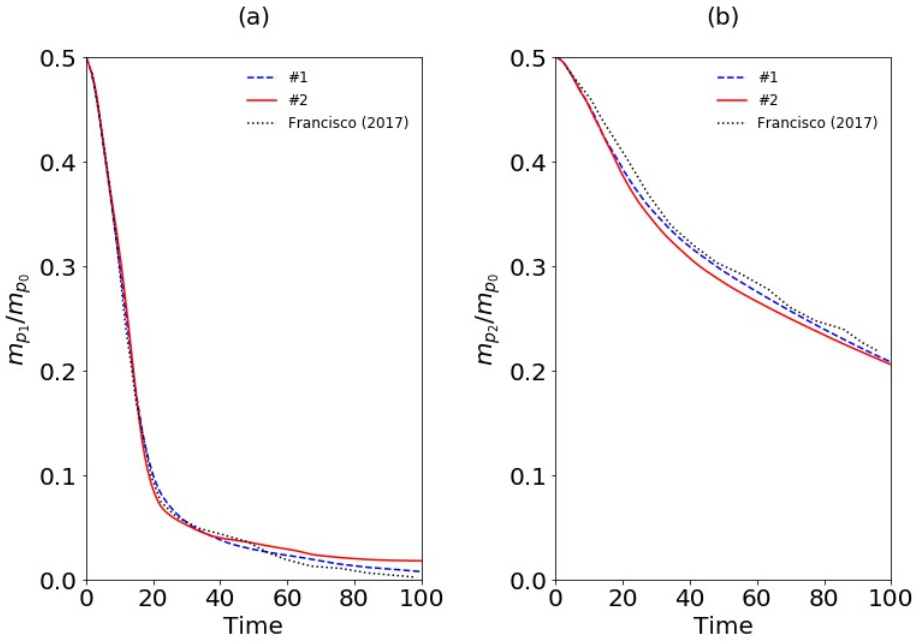

Figure 5. Suspended particles as function of time: (a) coarse fraction and (b) fine fraction. All curves are normalized by the initial mass suspended.

fine particle fraction, two phases can be also identified. However, the sedimentation rate grows proportionally to $\approx t^{0.75}$ and decreases at lower rate of $\approx t^{-1}$, after it reaches its peak at $t \approx 20$. Simulation $\#2$ has substantially higher sediment rate in the interval between $t \approx 4$ and $t \approx 8$, and between $t \approx 15$ and $t \approx 50$. Both simulations show lower sediment rates when compared with the reference. For the moment the only explanation for this difference is that the reference simulation is 2D.

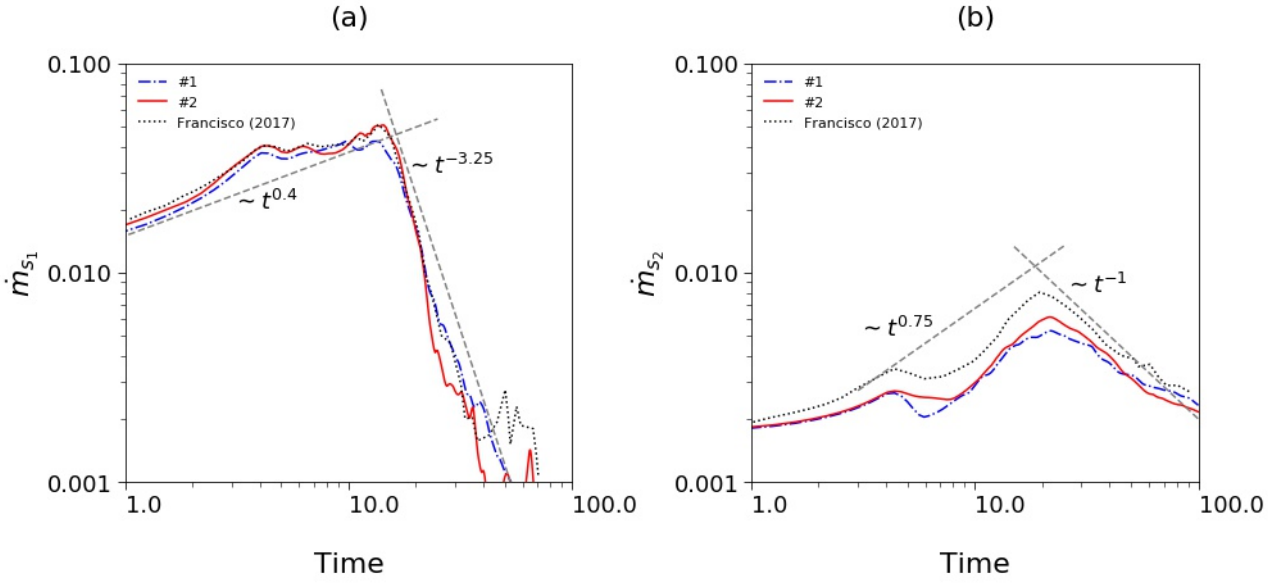

Figure 6. Sedimentation rate as a function of time: (a) coarse fraction and (b) fine fraction.

3.3 Deposit mean profile and composition

In Figure 7, the average profiles of deposit are plotted. The curves are normalized by final deposit at $t = 100$. There is a reasonable agreement between our results and the previous numerical and physical experiments. The peaks found in the deposit profile probably are related to the signature imposed by the strong Kelvin-Helmholtz vortexes mainly in quasi-2D simulations (Francisco *et al.*, 2017). It was observed that the deposit was formed close to the gate, which is common for this kind of configuration.

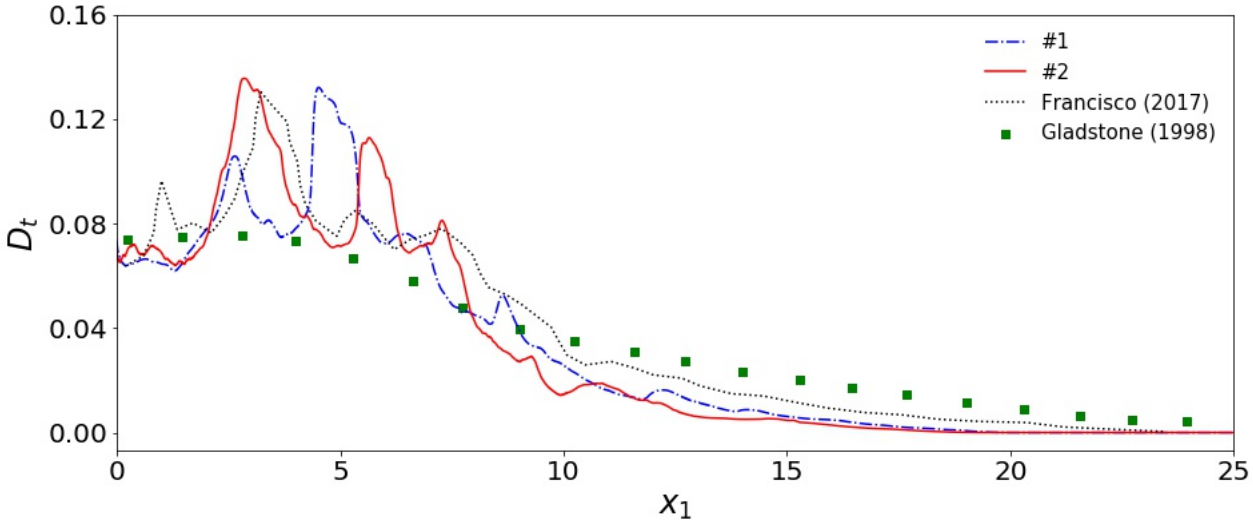

Figure 7. Final deposit profile for bi-disperse lock-exchange. All curves are normalized with the total deposit at the final time.

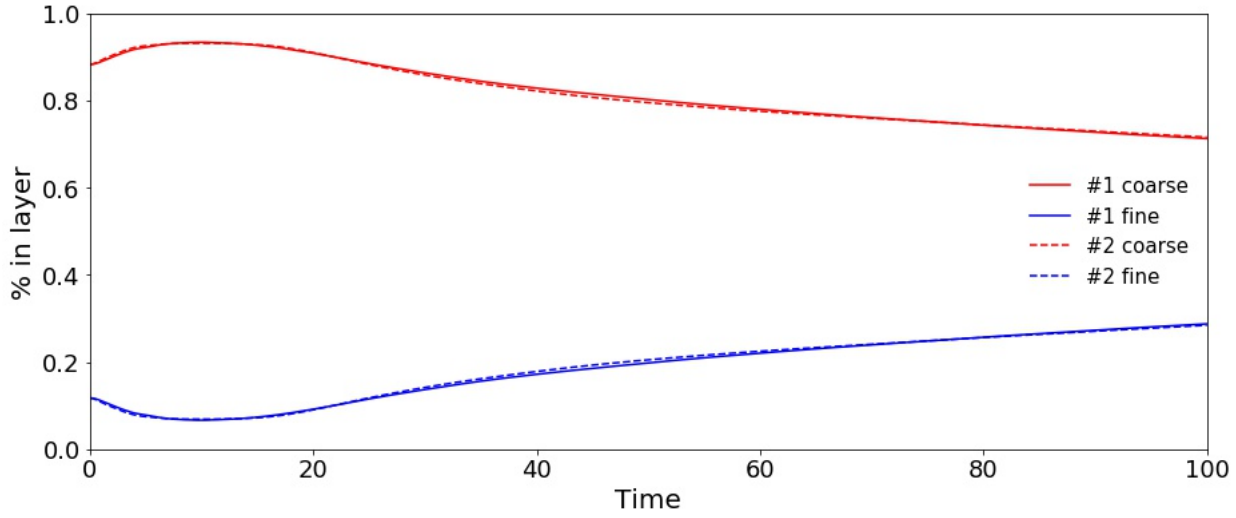

Figure 8. Temporal evolution of deposit composition for each particle fraction of simulations $\#1$ and $\#2$.

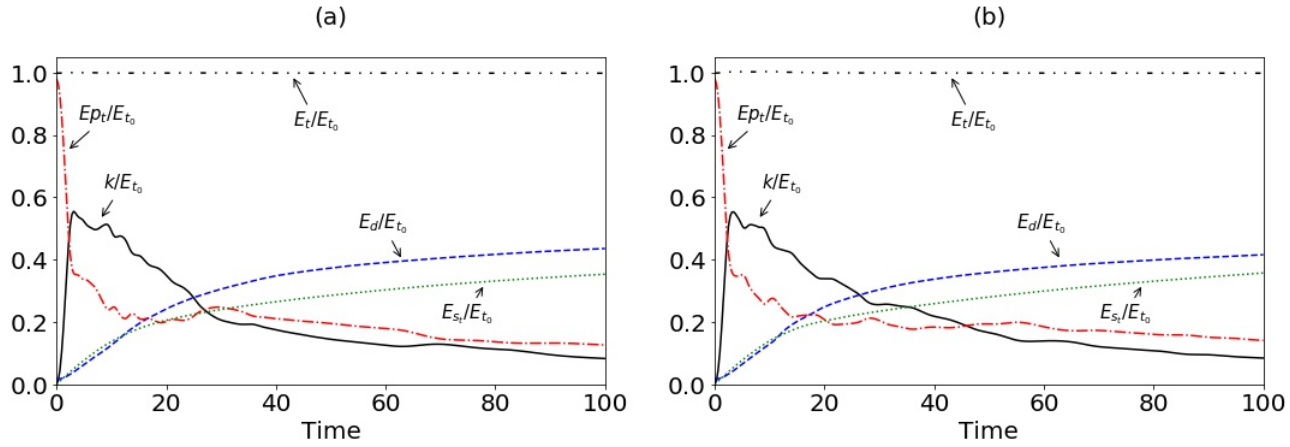

Figure 9. Temporal evolution of the energy for simulations (a) #1 and (b) #2. All curves are normalized with total initial energy (E_{t_0}).

Comparing the deposits of simulations $\#1$ and $\#2$, a difference in the configuration of the deposit, especially in the position of peaks, is identified. It could be a result of the difference in the temporal evolution of the front position between

the two simulations and the impact of double mass diffusivity. There is no significant difference between the distance reached for the two deposits.

In Figure 8 the temporal evolution of the deposit composition of each particle fraction for both simulations is plotted. Coarse particle concentration increases in the deposit during the beginning of the simulation, this situation persists until $t \approx 10$ when the concentration of fine particle starts growing in the deposit composition. This phenomenon occurs because the particles with high settling velocity sediments faster while the fine particles remain suspended for more time. As a consequence of that, the coarse particles should reduce in the composition of deposit along the time (Lucchese, 2018). At the end of the simulation time, the concentration of both particles approach to the initial concentration in the lock, what could be reached if simulations were carried out for a very long time. Furthermore, the deposit composition of the two simulations are very similar for most of the time, which means that the double mass diffusivity does not impact the deposit composition, at least for the parameters used.

3.4 Energy budget of the flow

Figure 9 shows the evolution of energy budget flow, for simulations $\#1$ and $\#2$, normalized by the total energy at the beginning of the simulation, observing conservation of the total energy. At the beginning of the simulations, the potential energy is maximum and after the gate is released, it suffers a drop while the kinetic energy has a fast increase, reaching its peak around $t \approx 3$. The kinetic energy after $t \approx 3$ decreases even with the potential energy decreasing. This happens because the two mechanisms of dissipation, the associated to convection E_d and to drag around the particles E_{s_t}, grow in importance along with the time evolution. The kinetic energy at $t = 100$ for simulations $\#1$ and $\#2$, respectively, are 8.28% and 8.42%, and the value for potential energy are 12.64% and 14.09%, respectively.

Comparing the two mechanisms of dissipation we notice that E_d has more impact in the energy loss. For simulations $\#1$ and $\#2$ the values of E_d are, respectively, 43.59% and 41.60%, while for E_{s_t} are 35.35% and 35.76%. It seems that the double diffusivity (simulation $\#2$) delays the conversion from potential to kinetic energy, since the respective curves only intercept at $t \approx 45$, in contrast to the unique difussitivity case where it occurs at $t \approx 25$.

4. CONCLUSION

We performed *DNS* of bi-disperse particle-laden gravity currents on a lock-exchange configuration with different values of Schmidt number for each particle fraction, to investigate the impact of double mass diffusivity on flow and deposit dynamics for a fixed Re number. Two simulations are considered in this study, the first one ($\#1$) with a unique Schmidt number for the two particle fractions, $Sc = 1$, while the second ($\#2$) possess the values $Sc = 3$ and $Sc = 1$ for coarse and fine particle fractions, respectively. We compared our results with physical and numerical experiments available in the literature, obtaining a fairly good agreement.

At the beginning of the simulation, the front position increases at a constant rate, with no effect of double mass diffusivity. At $t \approx 18$, when the streamwise movement is slowing down, a difference between the two simulations is identified, in which the flow with unique Schmidt number remains ahead when comparing with the other simulation. The time evolution of the front velocities for the two simulations are similar until $t \approx 18$, after this time the current front velocity of simulation $\#1$ is greater than the simulation $\#2$ for the most of the simulation time.

In terms of suspended material, the double mass diffusivity case shows lower fine particles suspended during the flow evolution. This impacts directly the flow movement because the fine particles are the most responsible for supporting the current motion. The final deposit agreed with the reference. The deposits has changed the configuration and position of the peaks for double mass diffusivity case. However, it seems that there is no perceptible effect of double diffusivity mass in the deposit composition. Finally, for the energy budget, it seems that in the double diffusive case the conversion from potential to kinetic energy is delayed, since the respective curves only intercept at $t \approx 45$, in contrast to the unique difussitivity case in which it occurs at $t \approx 25$.

5. ACKNOWLEDGEMENTS

We would like to thankful the Petrobras S. A. for his financial support to this research through the program SINAPSE, co-operation term N° 5900.0110995.19.9. We would like to grateful the CAPES - Coordenação de Aperfeiçoamento de Pessoal de Nível Superior - for his support through the program PROSUP - Programa de Suporte à Pós-Graduação de Instituições de Ensino Particulares. Also, we would like to grateful the Pontifical Catholic University of Rio Grande do Sul, PUCRS. Graduate Program in Materials Engineering and Technology - PGETEMA.

6. REFERENCES

Cantero, M.I., Lee, J.R., Balanchandar, S. and Garcia, M.H., 2007. "On the front velocity of gravity currents". *Journal of Fluid Mechanics*, Vol. 586, pp. 1–39.

Espath, L.F.R., Pinto, L.C., Laizet, S. and Silvestrini, J.H., 2014. "Two- and three-dimensional direct numerical simulation of particle-laden gravity currents". *Computers & Geosciences*, Vol. 63, pp. 9–16.

Farenzena, B.A., 2020. *Simulação numérica de correntes de densidade hiperpicnais sob referencial móvel*. Ph.D. thesis, Pontifícia Universidade Católica do Rio grande do Sul, Porto Alegre.

Francisco, E.P., Espath, L.F.R. and Silvestrini, J.H., 2017. "Direct numerical simulation of bi-disperse particle-laden gravity currents in the channel configuration". *Applied Mathematical Modelling*, Vol. 49, pp. 739–752.

Gladstone, C., Phillips, J.C. and Sparks, R.S.J., 1998. "Experiments on bidisperse, constant-volume gravity currents: propagation and sediment deposition". *Sedimentology*, Vol. 45, pp. 833–843.

Huppert, H.E. and Simpson, J.E., 1980. "The slumping of gravity currents". *Journal of Fluid Mechanics*, Vol. 99, pp. 785–799.

Kubo, Y., 2004. "Experimental and numerical study of topographic effects on deposition from two-dimensional, particle-driven density currents". *Sedimentary Geology*, Vol. 164, pp. 311–326.

Laizet, S. and Lamballais, E., 2009. "High-order compact schemes for incompressible flows: A simple and efficient method with quasi-spectral accuracy". *Journal of Computational Physics*, Vol. 228, pp. 5989–6015.

Laizet, S. and Li, N., 2011. "Incompact3d: A powerful tool to tackle turbulence problems with up to $o\left(10^5\right)$ computational cores". *International Journal for Numerical Methods in Fluids*, Vol. 67, pp. 1735–1757.

Lucchese, L.V., 2018. *Estudo numérico da sedimentação em correntes de turbidez com evolução do relevo de fundo*. Master's thesis, Universidade Federal do Rio Grande do Sul, Porto Alegre.

Manica, R., 2009. *Geração de Correntes de Turbidez de Alta Densidade: Condicionantes Hidráulicos e Deposicionais.* Ph.D. thesis, Universidade Federal do Rio Grande do Sul.

Meiburg, E. and Kneller, B., 2010. "Turbidity currents and their deposits". *Annual Review of Fluid Mechanics*, Vol. 42, pp. 135–156.

Nasr-Azadani, M.M., Meiburg, E. and Kneller, B., 2016. "Mixing dynamics of turbidity currents interacting with complex seafloor topography". *Environmental Fluid Mechanics*.

Necker, F., Härtel, C., Kleiser, L. and Meiburg, E., 2005. "Mixing and dissipation in particle-driven gravity currents". *Journal of Fluid Mechanics*, Vol. 545, pp. 339–372. ISSN 00221120. doi:10.1017/S0022112005006932.

Simpson, J.E., 1972. "Effects of the lower boundary on the head of a gravity current". *Annual Review of Fluid Mechanics*, Vol. 53, pp. 759–768.

Simpson, J.E., 1982. "Gravity currents in the laboratory, atmosphere, and ocean". *Annual Review of Fluid Mechanics*, Vol. 14, pp. 213–234.

Winters, K.B., Lombard, P.N., Riley, J.J. and D'Asaro, E.A., 1995. "Available potential energy and mixing in density-stratified fluids". *Journal of Fluid Mechanics*, Vol. 189, pp. 115–128.

7. RESPONSIBILITY NOTICE

The authors are the only responsible for the printed material included in this paper.